Smart Mater. Struct. **20** (2011) 094007 (8pp) doi:10.1088/0964-1726/20/9/094007

Enhanced aeroelastic energy harvesting by exploiting combined nonlinearities: theory and experiment

V C Sousa[1], M de M Anicézio[1], C De Marqui Jr[1] and A Erturk[2]

[1] Department of Aeronautical Engineering, Engineering School of Sao Carlos, University of Sao Paulo, São Carlos, SP 13566-590, Brazil
[2] G W Woodruff School of Mechanical Engineering, Georgia Institute of Technology, Atlanta, GA 30332-0405, USA

Received 19 April 2011, in final form 19 July 2011
Published 30 August 2011
Online at stacks.iop.org/SMS/20/094007

Abstract
Converting aeroelastic vibrations into electricity for low power generation has received growing attention over the past few years. In addition to potential applications for aerospace structures, the goal is to develop alternative and scalable configurations for wind energy harvesting to use in wireless electronic systems. This paper presents modeling and experiments of aeroelastic energy harvesting using piezoelectric transduction with a focus on exploiting combined nonlinearities. An airfoil with plunge and pitch degrees of freedom (DOF) is investigated. Piezoelectric coupling is introduced to the plunge DOF while nonlinearities are introduced through the pitch DOF. A state-space model is presented and employed for the simulations of the piezoaeroelastic generator. A two-state approximation to Theodorsen aerodynamics is used in order to determine the unsteady aerodynamic loads. Three case studies are presented. First the interaction between piezoelectric power generation and linear aeroelastic behavior of a typical section is investigated for a set of resistive loads. Model predictions are compared to experimental data obtained from the wind tunnel tests at the flutter boundary. In the second case study, free play nonlinearity is added to the pitch DOF and it is shown that nonlinear limit-cycle oscillations can be obtained not only above but also below the linear flutter speed. The experimental results are successfully predicted by the model simulations. Finally, the combination of cubic hardening stiffness and free play nonlinearities is considered in the pitch DOF. The nonlinear piezoaeroelastic response is investigated for different values of the nonlinear-to-linear stiffness ratio. The free play nonlinearity reduces the cut-in speed while the hardening stiffness helps in obtaining persistent oscillations of acceptable amplitude over a wider range of airflow speeds. Such nonlinearities can be introduced to aeroelastic energy harvesters (exploiting piezoelectric or other transduction mechanisms) for performance enhancement.

(Some figures in this article are in colour only in the electronic version)

1. Introduction

The transformation of aeroelastic vibrations into electrical energy is a simple and scalable option for wind energy harvesting. The goal is to enable aeroelastic configurations with electromechanical coupling for converting flow-induced structural vibrations into electricity. The harvested energy can be used for enabling self-powered small electronic components. The potential applications of interest for aeroelastic energy harvesting range from lifting components in aircraft structures to several other engineering problems involving wireless electronic components located in high wind areas. Aeroelastic energy harvesters can employ various transduction mechanisms that can be used for vibration-to-electricity conversion, such as the piezoelectric, electromagnetic, and electrostatic transductions covered in the literature of energy harvesting (Beeby *et al* 2006). However, due to the ease of application and high power density of

piezoelectric materials (Sodano *et al* 2004, Anton and Sodano 2007, Priya 2007, Cook-Chennault *et al* 2008), the recent papers on aeroelastic energy harvesting have mostly focused on the implementation of piezoelectric transduction.

Experimental investigation of power extraction from airflow excitation of a curved airfoil with macro-fiber composite (MFC) piezoelectric patches was reported by Erturk *et al* (2008). Time-domain modeling and simulations of cantilevered plates (in the form of an unswept wing) with embedded piezoceramic layers were presented by De Marqui *et al* (2009), (2010), (2011). The piezoaeroelastic wing model was obtained by combining an electromechanically coupled finite-element model (De Marqui *et al* 2009) with an unsteady vortex-lattice model. The effect of using segmented electrodes on the piezoaeroelastic response of the generator wing was also investigated. In another paper, frequency-domain piezoaeroelastic modeling and analysis of the same configuration (unswept generator wing with embedded piezoceramic layers) for energy harvesting were presented (De Marqui *et al* 2011) by using the doublet-lattice method. The resulting piezoaeroelastic equations were solved using a p–k scheme with electromechanical coupling and the evolutions of modal damping and frequency parameters with increasing airflow speed were analyzed. In these papers, wing-like configurations were investigated particularly for low power generation in unmanned aerial vehicle (UAV) applications.

Bryant and Garcia (2009) presented time-domain modeling of a 2-DOF typical section as a piezoelectric power harvester device driven by aeroelastic vibrations. The main motivation was to have an alternative energy source for placement in urban areas. A time-domain switching energy-extracting scheme was used in order to increase the power extraction from linear aeroelastic oscillations. Erturk *et al* (2010) presented a frequency-domain solution and experimental validations for a 2-DOF piezoaeroelastic energy harvester. The effect of piezoelectric power generation on the linear flutter speed was also discussed in the same paper along with the possible useful consequences of having nonlinearities in the system to create limit-cycle oscillations (LCOs) below the linear flutter speed. Some of the recent efforts include scalable configurations for wind energy harvesting. Zhu *et al* (2010) presented a small electromagnetic generator combining an airfoil attached to a cantilever and exposed to different flow conditions (free flow and wake behind a bluff body). Kwon (2010) proposed a T-shaped piezoelectric cantilever for energy harvesting from fluid flow. The experimental results show a flutter speed of around 4 m s^{-1}, which could be achieved under natural fluid flow.

A linear aeroelastic system undergoing persistent oscillations at the neutral stability condition (i.e. at the linear flutter speed) is the ideal linear scenario (De Marqui *et al* 2010, 2011, Erturk *et al* 2010). However, persistent oscillations occurring at a specific wind speed restrict the operating envelope of the energy harvester and often inherent nonlinearities are present. Nonlinear systems present a very rich variety of dynamic behavior such as LCOs, internal resonances, and chaotic motion (Nayfeh and Mook 1979, Moon 1987). In particular, stable aeroelastic LCOs of acceptable amplitude can provide an important source of persistent electrical power over a wide range of airflow speeds. Many authors have examined the aerodynamic and structural nonlinearities of aeroelastic systems (see, for instance, Lee *et al* 1999), while the focus in the present paper is placed on structural nonlinearities. For their simplicity and the fundamental insight they provide, aeroelastic typical section (airfoil) models have been widely studied. Price *et al* (1994) investigated free play nonlinearities in the pitch DOF of a typical section. Nonlinear LCO regions below the linear flutter speed were verified along with the subcritical behavior. Tang and Dowell (2006) also modeled free play nonlinearity in the pitch DOF of a typical section. In addition to the concentrated structural nonlinearity, they considered aerodynamic nonlinearities. Zhao and Yang (1990) examined LCOs when cubic nonlinearity is modeled in torsion DOF of an airfoil subjected to incompressible airflow. Zhao and Hu (2004) performed aeroelastic analysis of a two-dimensional airfoil section with combined geometric nonlinearities (free play and cubic stiffening) in the pitch DOF. A detailed discussion on the subject was presented by Lee *et al* (1999) and a review article due to Dowell and Tang (2002).

In this paper, linear and nonlinear modeling of a 2-DOF piezoaeroelastic section is presented with the eventual goal of exploiting combined nonlinearities in wind energy harvesting. The piezoelectric coupling is introduced through the plunge DOF while the nonlinearities are introduced to the pitch DOF. Three case studies are presented for energy harvesting from aeroelastic vibrations. First the interaction between piezoelectric power generation and linear aeroelastic response is investigated for a set of resistive loads at the flutter boundary. The predictions of the flutter boundary and the power output are verified against the experimental results obtained from wind tunnel tests. Secondly, free play nonlinearity is modeled in the pitch DOF and introduced to the experimental setup. It is known that the presence of a free play nonlinearity often results in subcritical bifurcations with LCOs at airflow speeds below the linear flutter speed (Dowell and Tang 2002), which is usually catastrophic in real aircraft but can be exploited for reducing the cut-in speed in aeroelastic energy harvesters. Theoretical predictions are compared to the experimental results and the favorable effect of having a free play on reducing the cut-in speed on nonlinear LCOs is shown. Finally, the free play and the cubic hardening nonlinearities are combined in the same DOF. The nonlinear piezoaeroelastic response is investigated over a range of airflow speeds and a range of nonlinear-to-linear spring constant ratios. The advantage of using combined free play and cubic nonlinearities is shown for obtaining nonlinear LCOs of acceptable amplitude over a range of airflow speeds.

2. Piezoaeroelastic model with combined nonlinearities

Figure 1 shows the schematic of a linear 2-DOF typical section. The plunge and the pitch displacement variables are denoted by h and α, respectively. The plunge displacement is measured at the elastic axis (positive in the downward direction) and the

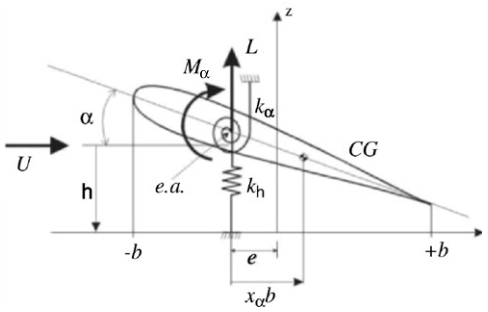

Figure 1. 2-DOF typical aeroelastic section under airflow excitation.

pitch angle is measured about the elastic axis (positive in the clockwise direction). In addition, b is the semichord length of the airfoil section, e is the distance of the elastic axis from the mid-chord position, x_α is the dimensionless chordwise offset of the elastic axis from the centroid (CG), k_h is the stiffness per length in the plunge DOF, k_α is the stiffness per length in the pitch DOF, b_h is the damping coefficient per length in the plunge DOF, b_α is the damping coefficient per length in the pitch DOF, and U is the airflow speed.

The well-known typical section model shown in figure 1 is modified in this work in two respects. First, piezoelectric coupling is added to the plunge DOF of the typical section and the resultant of the electrodes is connected to a resistive load. Second, concentrated nonlinearities (free play, cubic, and their combination) are added to the pitch DOF. After these modifications, the nonlinear piezoaeroelastic equations are obtained as

$$(m + m_e)\ddot{h} + S_\alpha \ddot{\alpha} + b_h \dot{h} + k_h h - \theta v_p / l = -L \tag{1}$$

$$S_\alpha \ddot{h} + I_\alpha \ddot{\alpha} + b_\alpha \dot{\alpha} + k_\alpha \alpha + f_{fp}(\alpha) + f_c(\alpha) = M_\alpha \tag{2}$$

$$C_p^{eq} \dot{v}_p + \frac{v_p}{R_l} + \theta \dot{h} = 0 \tag{3}$$

where m is the airfoil mass per length (in the span direction), m_e is the fixture mass (connecting the airfoil to the plunge springs) per length, I_α is the moment of inertia per length about the elastic axis, S_α is the static moment per length, l is the span length, R_l is the load resistance in the electrical domain, v_p is the voltage across the resistive load, C_p^{eq} is the equivalent capacitance of the piezoceramic layers, θ is the electromechanical coupling, M_α is the aerodynamic moment per length, L is the aerodynamic lift per length, and the overdot represents differentiation with respect to time. In equations (1)–(3), the nonlinear restoring moments $f_{fp}(\alpha)$ and $f_c(\alpha)$ are given by

$$f_{fp}(\alpha) = \begin{cases} -k_\alpha \alpha_{fp} \\ 0 \\ k_\alpha \alpha_{fp} \end{cases}$$

$$f_c(\alpha) = \begin{cases} k_{n\alpha}(\alpha - \alpha_{fp})^3 & \alpha > \alpha_{fp} \\ 0 & -\alpha_{fp} \leqslant \alpha \leqslant \alpha_{fp} \\ k_{n\alpha}(\alpha + \alpha_{fp})^3 & \alpha < -\alpha_{fp} \end{cases} \tag{4}$$

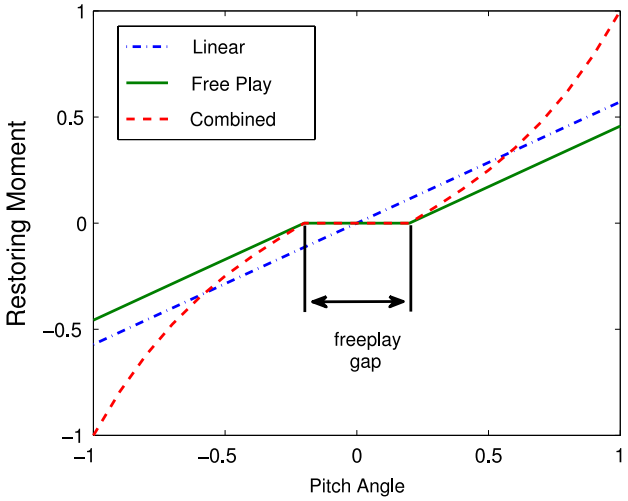

Figure 2. Restoring moments in the pitch DOF for the linear, the free play, and the combined free play and cubic nonlinearity configurations.

where α_{fp} is the semi-free play gap and $k_{n\alpha}$ is the nonlinear spring constant. It is important to note that when $k_{n\alpha} = 0$ and $\alpha_{fp} \neq 0$ the free play nonlinearity is obtained (combining the linear restoring moment and $f_{fp}(\alpha)$) whereas the $k_{n\alpha} \neq 0$ and $\alpha_{fp} \neq 0$ conditions yield the combined nonlinearity (combining the linear restoring moment, $f_{fp}(\alpha)$, and $f_c(\alpha)$). The linear equations are recovered when $\alpha_{fp} = 0$ and $k_{n\alpha} = 0$. The restoring moments in the pitch DOF for the linear, the free play, and the combined free play and cubic nonlinearity configurations are presented in figure 2.

The linear form of the piezoaeroelastic equations can be represented in the state-space form proposed by Edwards *et al* (1979) for the corresponding aeroelastic problem. However, due to the presence of the electromechanical coupling, the voltage output should be considered as an additional state variable. The unsteady aerodynamic loads (lift and moment terms in equations (1) and (2)) due to arbitrary motions are obtained from Jones' approximation of Wagner's indicial function, which is an approximation to the generalized Theodorsen function. Following the Laplace transformation of the governing equations, the aerodynamic load expressions for arbitrary values of the Laplace variable s are obtained from the representation for simple harmonic loads as rational functions of s. The Laplace inversion integral is employed and the rational functions describing the aerodynamic loads are ordinary differential equations that can be cast into the state-space form. Therefore two augmented states ($\mathbf{x}_a^t = \{x_1 \quad x_2\}$, where the superscript t stands for the transpose) are included in the state-space representation of the piezoaeroelastic problem. The linear state-space piezoaeroelastic equation is

$$\begin{bmatrix} \mathbf{I} & \mathbf{0} & \mathbf{0} & 0 \\ \mathbf{0} & \tilde{\mathbf{M}} & \mathbf{0} & 0 \\ \mathbf{0} & \mathbf{0} & \mathbf{I} & 0 \\ \mathbf{0} & \mathbf{0} & \mathbf{0} & C_p^{eq} \end{bmatrix} \begin{Bmatrix} \dot{\mathbf{x}} \\ \ddot{\mathbf{x}} \\ \dot{\mathbf{x}}_a \\ \dot{v}_p \end{Bmatrix} = \begin{bmatrix} \mathbf{0} & \mathbf{I} & \mathbf{0} & 0 \\ -\tilde{\mathbf{K}} & -\tilde{\mathbf{B}} & \mathbf{D} & \mathbf{\Theta}_1 \\ \mathbf{E}_1 & \mathbf{E}_2 & \mathbf{F} & 0 \\ \mathbf{0} & \mathbf{\Theta}_2 & \mathbf{0} & 1/R_l \end{bmatrix} \begin{Bmatrix} \mathbf{x} \\ \dot{\mathbf{x}} \\ \mathbf{x}_a \\ v_p \end{Bmatrix} \tag{5}$$

where $\mathbf{\Theta}_1 = \{0 \quad \theta/l\}^t$, $\mathbf{\Theta}_2 = \{0 \quad -\theta\}$, $\mathbf{x} = \{\alpha \quad \bar{h}\}^t$, and $\mathbf{I}$ is the 2×2 identity matrix. The mass, stiffness, and damping related matrices in equation (5) are

$$\tilde{\mathbf{M}} = \mathbf{M} - \frac{\rho b^2}{m}\mathbf{M}_{nc} \tag{6}$$

$$\tilde{\mathbf{K}} = \mathbf{K} - \frac{\rho b^2}{m}(U/b)^2\left(\mathbf{K}_{nc} + \frac{1}{2}\mathbf{R}\mathbf{S}_1\right) \tag{7}$$

$$\tilde{\mathbf{B}} = \mathbf{B} - \frac{\rho b^2}{m}(U/b)\left(\mathbf{B}_{nc} + \frac{1}{2}\mathbf{R}\mathbf{S}_2\right) \tag{8}$$

where $\mathbf{M}$ is the structural mass matrix, $\mathbf{B}$ is the structural damping matrix, $\mathbf{K}$ is the structural stiffness matrix, ρ is the air density, and $\mathbf{M}_{nc}$, $\mathbf{B}_{nc}$, and $\mathbf{K}_{nc}$ are noncirculatory aerodynamic matrices related to inertia, damping, and stiffness. These matrices as well as the aerodynamic matrices $\mathbf{D}$, $\mathbf{E}_1$, $\mathbf{E}_2$, $\mathbf{F}$, $\mathbf{R}$, $\mathbf{S}_1$, and $\mathbf{S}_2$ are given in Edwards *et al* (1979).

Equation (5) can be also represented as

$$\dot{\tilde{\mathbf{x}}} = \mathbf{A}\tilde{\mathbf{x}} \tag{9}$$

where

$$\mathbf{A} = \begin{bmatrix} \mathbf{0} & \mathbf{I} & \mathbf{0} & 0 \\ -\tilde{\mathbf{M}}^{-1}\tilde{\mathbf{K}} & -\tilde{\mathbf{M}}^{-1}\tilde{\mathbf{B}} & \tilde{\mathbf{M}}^{-1}\mathbf{D} & \tilde{\mathbf{M}}^{-1}\mathbf{\Theta}_1 \\ \mathbf{E}_1 & \mathbf{E}_2 & \mathbf{F} & 0 \\ \mathbf{0} & (1/C_p^{eq})\mathbf{\Theta}_2 & \mathbf{0} & (1/C_p^{eq})(1/R_l) \end{bmatrix} \tag{10}$$

$$\tilde{\mathbf{x}} = \{\mathbf{x} \quad \dot{\mathbf{x}} \quad \mathbf{x}_a\}^t. \tag{11}$$

A similar derivation can be applied when concentrated nonlinearities are present. In such a case, a combination of linear state-space models is used to represent the nonlinear system (Conner *et al* 1996). Therefore, the nonlinear state-space representation is

$$\dot{\tilde{\mathbf{x}}} = \mathbf{A}_i\tilde{\mathbf{x}} + \mathbf{a}_i + \mathbf{b}_i \tag{12}$$

where the state matrix and the vectors $\mathbf{a}_i$ and $\mathbf{b}_i$ change as the system reaches the free play boundaries (figure 2). The equations are solved using a Runge–Kutta algorithm with Henon's method (Henon 1982). Conner *et al* (1996) presented the adaptation of Henon's method to determine the switching point (or free play boundaries) in the time domain to avoid errors in numerical integration and numerical instability.

3. Case studies and model validation

This section presents three case studies using the piezoaeroelastic model described in section 2. The set of resistive loads considered here is $R_l = 10^2$, 10^3, 10^4, 10^5, and 10^6 Ω. In the first case study, the linear piezoaeroelastic solution is verified against the experimental piezoaeroelastic results obtained from wind tunnel tests at the flutter boundary. Secondly, bilinear structural stiffness is considered in the pitch DOF through the free play nonlinearity. In the presence of the free play, the torsional stiffness is zero for small airfoil rotations (due to the free play gap) and it approaches the original linear torsional stiffness for relatively large rotations (figure 2). In the third case study, a combined nonlinearity is considered in the pitch DOF. For small airfoil rotations, the torsional stiffness is zero and a stiffening behavior is observed for large rotations as in figure 2. The piezoaeroelastic behavior is investigated for the same set of resistive loads and also for a range of nonlinear-to-linear pitch stiffness ratios ($\eta = k_{n\alpha}/k_\alpha$) defined based on the spring constants in equation (2).

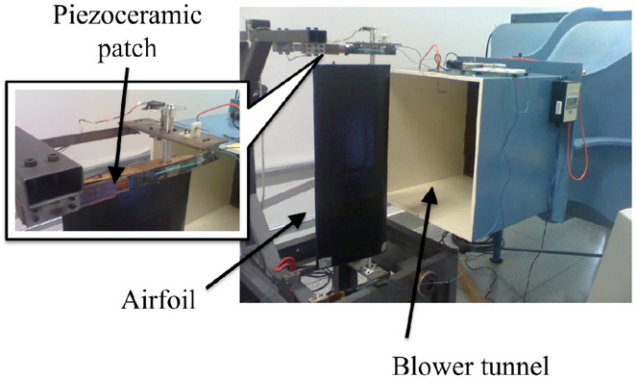

Figure 3. Experimental typical section and detailed view of the piezoceramic patches on the plunge springs.

Table 1. Properties of the piezoaeroelastic typical section.

b	0.125 m
l	0.5 m
μ	2.597
x_α	0.260
r_α	0.504
ω_h	52.2 rad s^{-1}
ω_α	26.6 rad s^{-1}
ζ_h	0.0035
ζ_α	0.088

Figure 3 shows the experimental setup used for investigating the linear and nonlinear piezoaeroelastic behavior of the typical section. This setup is a typical aeroelastic section modified with piezoelectric coupling and was not originally designed for energy harvesting (however, the results are applicable to its scaled versions). The plunge stiffness is due to the four elastic beams with clamped–clamped end conditions shown in the detailed views of figure 3. The free ends of the elastic beams are connected to metal plates at the top and the bottom. Therefore the experimental setup in this work slightly deviates from the ideal definition of a typical section (where springs are assumed massless), yielding the fixture mass (m_e) defined in equation (1). A shaft (or pitch axis) is mounted to the upper and the lower plates through a pair of bearings. The pitch stiffness is given by a spring wire clamped into the shaft (at the elastic axis). The free end of the wire is simply supported on the top plate (without a gap for the linear case and with a gap for the free play nonlinearity). Two piezoceramic patches (QP10N from Mide Technology Corporation) are attached onto the root of two bending stiffness members (symmetrically) and their electrodes are connected in parallel to the external resistive load.

The properties of the piezoaeroelastic typical section are shown in table 1. The dimensionless aeroelastic parameters

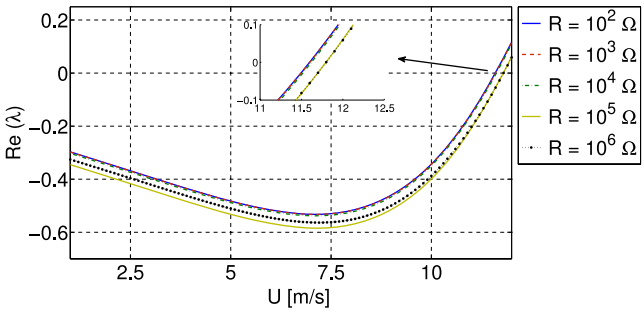

Figure 4. Real part of the eigenvalue (for the mode that becomes unstable) with increasing airflow speed for a set of resistive loads along with a close-up view around the flutter boundary.

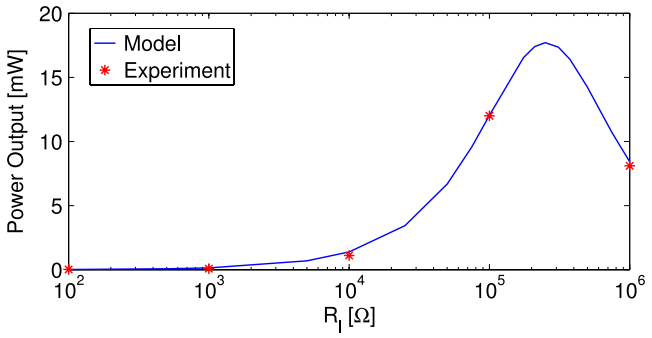

Figure 5. Experimental and theoretical power outputs versus load resistance at the linear flutter boundary.

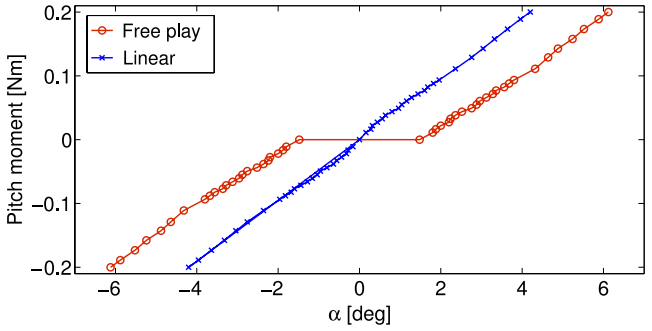

Figure 6. Experimentally measured linear and bilinear (free play) pitching moments.

in this table are defined as the mass ratio, μ, the radius of gyration, r_α, and the pitch and plunge damping ratios, ζ_α and ζ_h, respectively (the definitions of these dimensionless parameters can be found in textbooks on aeroelasticity, e.g., Hodges and Pierce 2002). The uncoupled and undamped pitch and plunge frequencies are ω_α and ω_h, respectively. The manufacturer's published equivalent capacitance of $C_p^{eq} = 120$ nF is used in the piezoaeroelastic model. The electromechanical coupling parameter is obtained based on distributed parameter modeling (Erturk and Inman 2009) by considering clamped–clamped end conditions for the two beams with piezoceramic patches as $\theta = 1.55$ mN V^{-1} (Erturk *et al* 2010).

3.1. Linear piezoaeroelastic typical section

In the first case study, the linear aeroelastic behavior of the electromechanically coupled typical section is investigated at the flutter boundary for a set of resistive loads. The real part of the relevant eigenvalue λ is shown in figure 4 for changing airflow speed and different resistive loads. Only the eigenvalue for the mode that becomes unstable is shown for clarity. The predicted linear short-circuit ($R_l \to 0$) flutter speed is 11.6 m s^{-1}. The experimental short-circuit flutter speed is measured as 11.9 m s^{-1}. The load resistance of 100 kΩ gives the maximum experimental power output among the set of resistors considered in this paper. The model predicts the linear flutter speed for this load as 11.8 m s^{-1}. The experimental flutter speed for the same resistive load is 12.1 m s^{-1}. Although the model slightly underestimates the experimental flutter speed, approximately the same increase (1.7%) in the linear flutter speed (with respect to the short-circuit flutter speed) is observed for the resistive load of 100 kΩ. It is also interesting to note in figure 4 that approximately the same flutter speed (11.8 m s^{-1}) is obtained for load resistance values of 100 kΩ and 1 MΩ.

The variation of power output with increasing load resistance is shown in figure 5. The electrical power is experimentally measured as close as possible to the linear flutter speed of each resistive load (in order to obtain almost persistent oscillations but to avoid post-flutter oscillations). The model slightly overestimates the experimental power output for the set of resistive loads used in this work. The predicted power output for the load resistance of 100 kΩ is 13.8 mW and the experimental power output for the same load is measured as 12 mW. This overestimation can be attributed to material nonlinearities and nonlinearities in dissipation (Stanton *et al* 2010a, 2010b) not considered in this work. The post-flutter response of the particular experimental setup results in dramatically large-amplitude oscillations with growing amplitude (of divergent and oscillatory nature for practical purposes) since the setup behaves quite linearly around the flutter speed. Therefore, the maximum airflow speed of effective energy harvesting without growing oscillations is very close to the linear flutter speed. However, almost persistent oscillations occurring at a specific wind speed restrict the operating envelope of the linear flow energy harvester.

3.2. Piezoaeroelastic typical section with a free play

The experimental piezoaeroelastic typical section with free play nonlinearity is tested next. The nonlinear piezoaeroelastic behavior of the coupled typical section is investigated for the same set of resistors. The free play gap causing the bilinear stiffness in the pitch DOF is $\pm 1.4°$ ($\alpha_{fp} = 1.4\pi/180$ rad). The linear pitch stiffness outside the free play gap is given by the same stiffness as the linear case study. The experimental linear pitching moment and free play pitching moment are shown in figure 6.

In the presence of free play nonlinearity, the LCO mechanism observed in the experiments is due to subcritical bifurcations (Nayfeh and Balachandran 1995), leading to

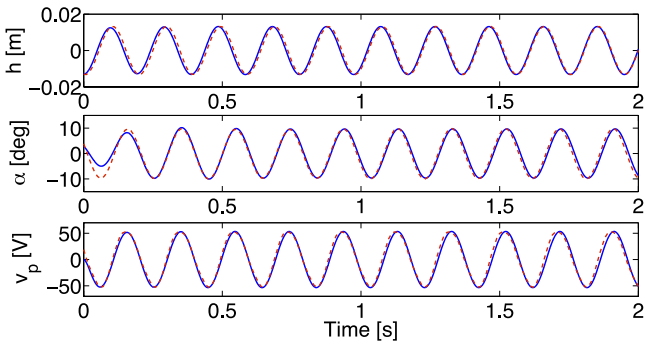

Figure 7. Experimental (dashed line) and theoretical (solid line) nonlinear piezoaeroelastic response histories for $R_l = 100$ kΩ (experiment: 10.0 m s^{-1}, model: 10.4 m s^{-1}).

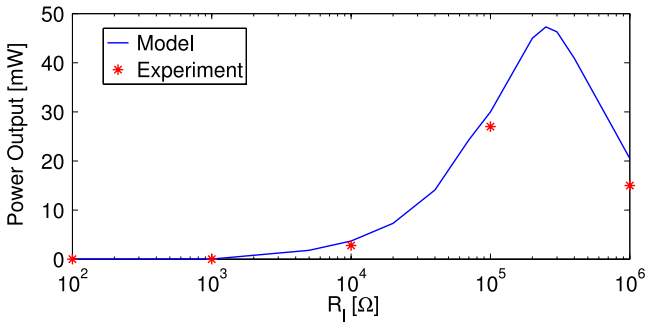

Figure 8. Experimental and theoretical power outputs versus load resistance (experiment: 10.0 m s^{-1}, model: 10.4 m s^{-1}).

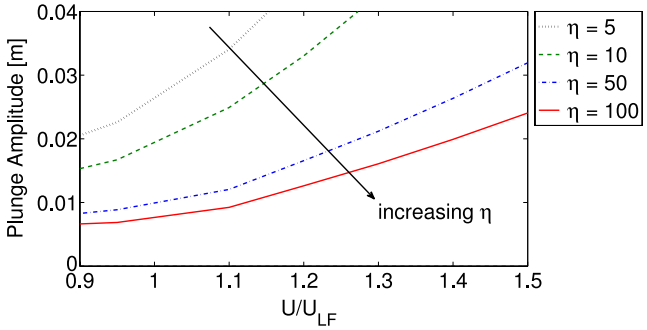

Figure 9. Plunge amplitude with increasing airflow speed for three different values of the nonlinear-to-linear stiffness ratio ($R_l = 100$ Ω).

LCOs below the linear flutter speed of each load resistance used in this work. The lowest airflow speed to have LCO is experimentally measured as 10.0 m s^{-1} and the model predicts this lower bound as 10.4 m s^{-1}. It is observed that, beyond 12.0 m s^{-1}, the response amplitude (predicted by the present model) becomes very large for all resistive loads considered here. Therefore, no experimental testing was performed outside the range of 10.0–12.0 m s^{-1}.

The load resistance of 100 kΩ gives the maximum experimental power output among the set of resistors used in this case as well. The piezoaeroelastic time histories (pitch, plunge, and voltage output) for this resistive load with persistent oscillations are shown in figure 7. The model predicts the amplitudes of the pitch, plunge, and voltage response histories as well as the frequencies accurately.

The power versus load resistance diagrams obtained from the experiments and the model are displayed in figure 8. In this figure, the experimental and theoretical airflow speeds of LCO are 10.0 m s^{-1} and 10.4 m s^{-1}, respectively. Unlike the case of response at the linear flutter boundary (figure 5), the LCO due to free play (figure 8) is a strongly nonlinear phenomenon and the airflow speed of persistent oscillations is not affected by the resistive shunt damping effect of piezoelectric power generation since piezoelectric coupling is a weak coupling in the system, usually of the order of mechanical damping (Erturk and Inman 2011). Moreover, in this particular case, the piezoelectric coupling is more effective on the plunge DOF while the strong nonlinearity is in the pitch DOF. Therefore, all the experimental and theoretical data points in figure 8 are for the airflow speeds of 10.0 m s^{-1} and 10.4 m s^{-1}, respectively. The maximum experimental power output is again obtained for $R_l = 100$ kΩ. For this electrical load, the power output is predicted by the model as 28.6 mW, slightly overestimating the experimental value of 27.0 mW. Note that the maximum power output for this configuration with free play nonlinearity is more than twice the power output obtained in the previous case study (linear piezoaeroelastic power harvester excited at the flutter boundary). Moreover, the cut-in speed of LCO is reduced with the free play nonlinearity by about 2 m s^{-1}. However, the range of airflow speeds with LCO of acceptable amplitude is still relatively narrow. Therefore, it is required to reduce the response amplitude to acceptable values while keeping the free play nonlinearity, which is theoretically investigated in section 3.3.

3.3. Piezoaeroelastic typical section with combined nonlinearities

Having validated the nonlinear piezoaeroelastic energy harvester model, the configuration with combined free play and hardening cubic stiffness nonlinearities (recall figure 2) is studied in this section. The theoretical piezoaeroelastic behavior of the electromechanically coupled typical section is investigated for different values of the nonlinear-to-linear stiffness ratio ($\eta = k_{nl}/k_\alpha$). The free play gap considered in this third case study is ±1.4° as in section 3.2. The vibration amplitude and the electrical power output are investigated for airflow speeds ranging from 90% to 150% of the linear flutter speed of 12 m s^{-1}.

Figure 9 shows the plunge amplitude with dimensionless airflow speed (the ratio of airflow speed to linear flutter speed) close to short-circuit conditions ($R_l = 100$ Ω). It is clear from figure 9 that the plunge amplitude is highly sensitive to the nonlinear-to-linear stiffness ratio. When $\eta = 0$ (i.e., $k_{nl} = 0$) and $\alpha_{fp} \neq 0$, the free play nonlinearity is achieved. The amplitude of plunge displacement increases with increasing airflow speed and decreases with increasing stiffness ratio. Therefore, for the configuration with combined nonlinearity ($\eta \neq 0$ and $\alpha_{fp} \neq 0$), the LCO response has acceptable amplitude over a wide airflow speed range. In practice, the nonlinear-to-linear stiffness ratio can be increased by

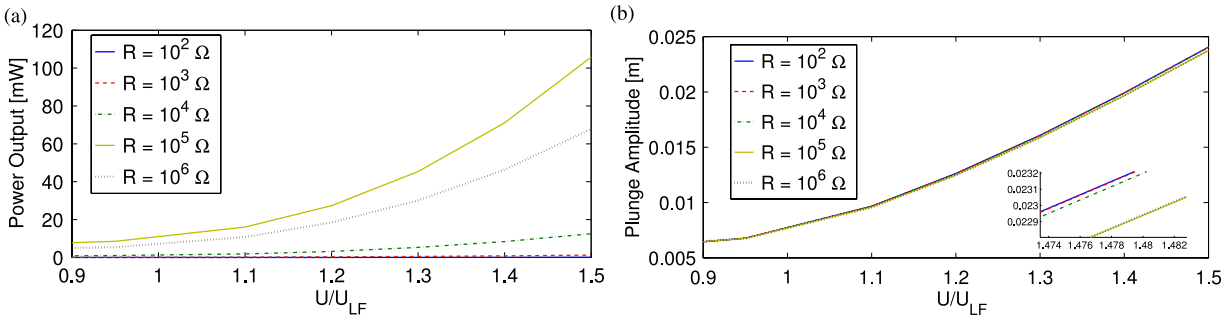

Figure 10. Variations of (a) the power output and (b) the plunge amplitude with airflow speed for five different values of load resistance ($\eta = 100$).

employing additional inherently nonlinear hardening springs to improve the range of airflow speeds with acceptable response amplitude in the presence of free play nonlinearity.

For the case of $\eta = 100$, the variation of the electrical power output with increasing airflow speed for five different values of load resistance is shown in figure 10(a). The power output increases with increasing airflow speed for any resistive load. At any airflow speed, as the value of load resistance is increased from $R_l = 100\ \Omega$ to 100 kΩ, the power output increases. When the value of load resistance is further increased to $R_l = 1$ MΩ (close to the open-circuit condition) the power output starts decreasing. Therefore, among the set of resistive loads considered here, $R_l = 100$ kΩ gives the maximum power output over the entire range of airflow speeds. The maximum theoretical power of 106 mW is obtained for the optimum load resistance at $U = 18$ m s^{-1} ($U/U_{LF} = 1.5$), which is expected to overestimate the possible experimental results due to material and dissipative nonlinearities. Figure 10(b) shows the variation of plunge amplitude with airflow speed and $\eta = 100$ for the set of resistive loads considered in this work. The effect of power generation on the vibration amplitude is negligible for practical purposes, in agreement with the discussion given in section 3.2.

4. Conclusions

This paper investigates linear and nonlinear piezoaeroelastic energy harvesting theoretically and experimentally with a focus on the advantages of exploiting combined nonlinearities. The piezoelectric coupling is introduced through the plunge DOF while the concentrated structural nonlinearities are introduced to the pitch DOF. A state-space piezoaeroelastic model is derived and the unsteady aerodynamic loads are obtained from Jones' approximation of Wagner's indicial function, which is an approximation to the generalized Theodorsen function.

The linear piezoaeroelastic response predictions are successfully verified against experimental results obtained from wind tunnel tests at the flutter boundary. Although usually avoided in real aircraft, the response at the flutter boundary is the ideal scenario for energy harvesting from linear aeroelastic vibrations. However, having persistent oscillations only at the airflow speed of neutral stability is a very limited condition for aeroelastic energy harvesting. Nonlinearities exist often inherently within the system (and they are pronounced under certain conditions) or they can be introduced for performance enhancement.

Concentrated nonlinearities are introduced to the pitch DOF and the nonlinear piezoaeroelastic behavior of the electromechanically coupled typical section is also investigated. First, the free play nonlinearity is considered in the pitch DOF to reduce the cut-in speed of persistent oscillations. The predictions are successfully verified against the experimental measurements. The presence of free play nonlinearity results in LCOs at airflow speeds below the linear flutter speed (reducing the cut-in speed by about 2 m s^{-1}), which is a favorable condition in energy harvesting. The maximum power output of the configuration with free play nonlinearity is observed to be twice that of the linear configuration (at the flutter boundary). In both cases (linear and free play) divergent oscillations are observed at airflow speeds above the linear flutter speed (12 m s^{-1}).

In order to obtain persistent and bounded oscillations of acceptable amplitude in the presence of free play nonlinearity, hardening cubic stiffness is combined with free play nonlinearity in the pitch DOF. Having validated the model for the linear and the free play configurations in two case studies, simulations are performed to study the effect of combined nonlinearities. The piezoaeroelastic behavior is investigated for a range of nonlinear-to-linear pitching stiffness ratios and resistive loads. The response amplitudes increase with increasing airflow speed and decrease with increasing nonlinear-to-linear stiffness ratio. Overall, it is shown that the free play nonlinearity reduces the cut-in speed and the hardening stiffness helps in bringing the response amplitude to acceptable levels (hence increasing the upper limit of the post-flutter speed of acceptable response amplitude). Therefore, the combination of the free play and the hardening cubic stiffness nonlinearities constitutes the most useful scenario for aeroelastic energy harvesting. This conclusion is applicable to aeroelastic energy harvesters employing other transduction mechanisms as well.

Acknowledgments

The authors gratefully acknowledge CNPq and FAPEMIG for partially funding the present research work through the INCT-

EIE. The authors also gratefully acknowledge the support from CNPq (558646/2010-7 and 484132/2010-5).

References

Anton S R and Sodano H A 2007 A review of power harvesting using piezoelectric materials 2003–2006 *Smart Mater. Struct.* **16** R1–21

Beeby S P, Tudor M J and White N M 2006 Energy harvesting vibration sources for microsystems applications *Meas. Sci. Technol.* **13** R175–95

Bryant M and Garcia E 2009 Development of an aeroelastic vibration power harvester *Proc. Active and Passive Smart Structures and Integrated Systems 2009*

Conner M D, Virgin L N and Dowell E H 1996 Accurate numerical integration of state space models for aeroelastic systems with free play *AIAA J.* **34** 2202–5

Cook-Chennault K A, Thambi N and Sastry A M 2008 Powering MEMS portable devices—a review of non-regenerative and regenerative power supply systems with emphasis on piezoelectric energy harvesting systems *Smart Mater. Struct.* **17** 043001

De Marqui C Jr, Erturk A and Inman D J 2009 An electromechanical finite element model for piezoelectric energy harvester plates *J. Sound Vib.* **327** 9–25

De Marqui C Jr, Erturk A and Inman D J 2010 Piezoaeroelastic modeling and analysis of a generator wing with continuous and segmented electrodes *J. Intell. Mater. Syst. Struct.* **21** 983–93

De Marqui C Jr, Vieira W G R, Erturk A and Inman D J 2011 Modeling and analysis of piezoelectric energy harvesting from aeroelastic vibrations using the doublet-lattice method *J. Vib. Acoust.* **133** 011003

Dowell E H and Tang D 2002 Nonlinear aeroelasticity and unsteady aerodynamics *AIAA J.* **40** 1697–707

Edwards J W, Ashley H and Breakwell J V 1979 Unsteady aerodynamic modeling for arbitrary motions *AIAA J.* **17** 365–74

Erturk A, Bilgen O, Fontenille M and Inman D J 2008 Piezoelectric energy harvesting from macro-fiber composites with an application to morphing wing aircrafts *Proc. 19th Int. Conf. of Adaptive Structures and Technologies (Monte Verità, Ascona, October 2008)*

Erturk A and Inman D J 2009 An experimentally validated bimorph cantilever model for piezoelectric energy harvesting from base excitations *Smart Mater. Struct.* **18** 025009

Erturk A and Inman D J 2011 *Piezoelectric Energy Harvesting* (Chichester, UK: Wiley)

Erturk A, Vieira W G R, De Marqui C and Inman D J 2010 On the energy harvesting potential of piezoaeroelastic systems *Appl. Phys. Lett.* **96** 184103

Henon M 1982 On the numerical computation of Poincaré maps *Physica* D **5** 512–4

Hodges D H and Pierce G A 2002 *Introduction to Structural Dynamics and Aeroelasticity* (New York: Cambridge University Press)

Kwon S D 2010 A T-shaped piezoelectric cantilever for fluid energy harvesting *Appl. Phys. Lett.* **77** 164102

Lee B H L, Price S J and Wong Y S 1999 Nonlinear aeroelastic analysis of airfoils: bifurcation and chaos *Prog. Aerospace Sci.* **35** 205–334

Moon F C 1987 *Chaotic Vibrations* (New York: Wiley)

Nayfeh A H and Balachandran B 1995 *Applied Nonlinear Dynamics* (New York: Wiley)

Nayfeh A H and Mook D T 1979 *Nonlinear Oscillations* (New York: Wiley)

Price S J, Lee B H K and Alighanbari H 1994 Postinstability behavior of a two-dimensional airfoil with a structural nonlinearity *J. Aircr.* **31** 1395–401

Priya S 2007 Advances in energy harvesting using low profile piezoelectric transducers *J. Electroceram.* **19** 167–84

Sodano H A, Inman D J and Park G 2004 A review of power harvesting from vibration using piezoelectric materials *Shock Vib. Dig.* **36** 197–205

Stanton S C, Erturk A, Mann B P and Inman D J 2010a Resonant manifestation of intrinsic nonlinearity within electroelastic micropower generators *Appl. Phys. Lett.* **97** 254101

Stanton S C, Erturk A, Mann B P and Inman D J 2010b Nonlinear piezoelectricity in electroelastic energy harvesters: modeling and experimental identification *J. Appl. Phys.* **108** 074903

Tang D and Dowell E H 2006 Flutter and limit-cycle oscillations for a wing-store model with freeplay *J. Aircraft* **43** 487–503

Zhang R and Singh S N 2001 Adaptive output feedback control of an aeroelastic system with unstructured uncertainties *J. Guid. Control Dyn.* **24** 502–9

Zhao Y H and Hu H Y 2004 Aeroelastic analysis of a non-linear airfoil based on unsteady vortex lattice model *J. Sound Vib.* **276** 491–510

Zhao L C and Yang Z C 1990 Chaotic motions of an airfoil with nonlinear stiffness in incompressible flow *J. Sound Vib.* **138** 245–54

Zhu D, Beeby S, Tudor J, White N and Harris N 2010 A novel miniature wind generator for wireless sensing applications *IEEE Sensors 2010 (November 2010, Waikoloa, Hawaii)*